Journal of Quantitative Spectroscopy & Radiative Transfer 243 (2020) 106821

Contents lists available at ScienceDirect

Journal of Quantitative Spectroscopy & Radiative Transfer

journal homepage: www.elsevier.com/locate/jqsrt

Radiation fields in radiative transfer: Spherical-wavelet representation

Guanglang Xu [a,*], Karri Muinonen [a,b]

[a] Department of physics, University of Helsinki, Finland
[b] Finnish Geospatial Research Institute FGI, National Land Survey of Finland, Finland

ARTICLE INFO

Article history:
Received 21 September 2019
Revised 27 December 2019
Accepted 29 December 2019
Available online 30 December 2019

Keywords:
Spherical wavelets
Spherical harmonics
Radiation fields
Discrete-ordinate methods
Radiative transfer

ABSTRACT

The spherical wavelet based on the lifting scheme is introduced for adaptive discrete-ordinate sampling of the radiation fields, particularly, in the radiative transfer computation using iterative schemes. The lifting scheme for wavelet transform is described from an implementation point of view, including the construction of hierarchical geodesic grids on the sphere and wavelet constructions. In addition, we compare the method with the conventional spherical harmonics, numerically investigating the transformation error and efficiency. The transformation matrices are built in the least-squares sense. The results demonstrate the feasibility of using spherical wavelets as an adaptive discrete-ordinate sampling method at the cost of $O(N)$, where N is the number of significant coefficients.

1. Introduction

Radiative transfer problems are often solved by introducing a directional numerical representation of the radiation fields [1–3]. There are a few commonly applied strategies for modeling the radiation fields, notably, the Monte Carlo [4,5], spherical-harmonics [6,7], and discrete-ordinate methods [8–11]. These methods all come with their shortcomings and advantages. The Monte Carlo methods are often regarded as the most accurate methods for 3-D radiative transfer simulations. But they have the drawback of producing statistical noise due to the stochastic nature of modeling the radiation field. To reduce the noise, one has to increase the number of samples, which makes the simulation computationally expensive. The spherical-harmonics methods represent the radiance by a weighted sum of spherical harmonics basis functions up to a truncation order [12,13]. The transfer equation can then be transformed into equations for the expansion coefficients of the harmonics. Because its solution is obtained in the spectral domain, it suffers from non-physical oscillations in non-smooth regimes, potentially giving negative values of the radiances. Perhaps the most commonly applied methods for solving the radiative transfer equation are the discrete-ordinate methods, thanks to their efficiency. With the discrete-ordinate representation, one can replace the integro-differential equation with a system of linear equations describing the discrete-streams approximation [14]. Although the discrete-ordinate methods can be implemented efficiently, they suffer from the so-called "ray effect" in multi-dimentional cases [15]. The ray effect is a consequence of approximating the continuously varying angular nature of radiation with a specific set of discrete directions, and is independent of the spatial discretization.

An example of using two of the aforementioned representations is the spherical-harmonics discrete-ordinate method (SHDOM), a widely used deterministic method for 3-D radiative transfer [16–20]. SHDOM solves 3-D radiative transfer equation based on an iteration scheme, i.e., updating the source term and radiance iteratively until all quantities satisfy the transfer equation everywhere. The source term is updated in the spherical-harmonics domain, while the radiance is updated in the discrete-ordinate domain. Therefore, a transformation needs to be made between the two representations.

Without considering the time-dependency and polarization, the solution phase space in radiative transfer problems for a single wavelength is generally 5-D, i.e., three for the spatial *XYZ*-domain and two being associated with the radiation propagation direction. Adaptivity in 3-D spatial grids has been implemented in methods such as SHDOM, which means that higher spatial resolution is provided wherever the source term is changing more rapidly. It improves the accuracy of the solution and the computation resources are distributed in a more reasonable way. On the other hand, the adaptivity on the angular domain has not yet been exploited and one often resorts to the Gaussian quadrature rules on the zenith angle. The Gaussian quadrature rules provide a fixed set of discrete-ordinates, in other words, no adaptivity for representing the varying radiation fields during the iteration process. In

* Corresponding author.
E-mail addresses: guanglang.xu@helsinki.fi (G. Xu), karri.muinonen@helsinki.fi (K. Muinonen).

https://doi.org/10.1016/j.jqsrt.2019.106821

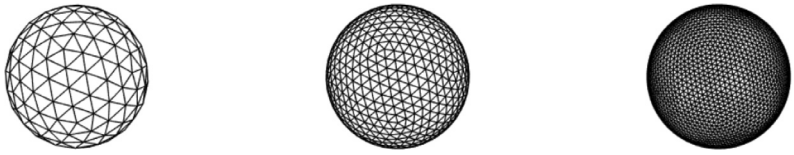

Fig. 1. The geodesic grids of three different levels.

particular, the quadrature rules have difficulties when they are used to evaluate regions with sharp gradients or discontinuities. Although the convergence may be achieved without any complications, the unseen spikes in an otherwise smooth function `max` produce different answers as the number, and so, the position of the quadrature angles is changed. Note that the abrupt changes in the angular distribution become especially large if the problem involves a small amount of diffuse scattering, because by scattering the radiation is redirected to new directions. In addition, SHDOM truncates the spherical harmonics series in accordance with the number of discrete ordinates, which may introduce oscillations (known as Gibb's errors) in the solution near the sharp features in the angular distribution. Clearly, the root of the difficulty is that a non-smooth radiance distribution is not well approximated by smooth functions that are chosen in advance. In principle, such difficulties may exist in any discrete ordinate methods with a fixed set of discrete ordinates.

In this paper, we introduce another discrete-ordinate sampling technique called spherical wavelets. The spherical wavelets are commonly used as a tool for data compression on the sphere [21–23], particularly in the computer graphics area. They provide adaptive representations of spherical functions in a discretized setting. The goals of the paper are twofold. First, we introduce the technique of spherical wavelets, particularly focusing on its implementation for adaptive discrete-ordinate sampling. Secondly, we numerically investigate the transformation between the spherical-harmonics and spherical-wavelets representations of the radiation fields, providing an essential basis for application in radiative transfer simulations.

2. Introduction to spherical wavelets

In wavelet analysis, there are a large number of wavelet functions and methods of transform suitable for different applications. Classically, wavelets on a real line (R) or plane (R^2) are constructed by dilating and translating a mother wavelet. However, extending this method of construction to the spherical surface(S^2) is quite difficult and not suited for discrete-ordinate sampling [24,25]. The lifting scheme, proposed by Shröder and Sweldens [21], is an efficient way to construct series of wavelets on the sphere. Particularly, it maintains many desirable properties of classical wavelets, such as localization, vanishing moments, and fast transform. The main purpose of the section is to explain the lifting scheme for constructing the spherical wavelet. For the readers who would like to know more about the implementation details and develop their own wavelets code for radiative transfer, a Matlab wavelet tool box developed by G. Peyre is recommended [26]. For more detailed explanation on the principle of the lifting scheme, see Daubechies et al. [27]. The notation used in paper is partly motivated by Hu et al. [28].

2.1. The construction of hierarchical geodesic grids on the sphere

The spherical wavelets are constructed on hierarchical geodesic grids on the sphere. These grids can be obtained by a recursive subdivision of the zero-level grid, the icosahedron. Fig. 1 shows the example of three different levels of geodesic grids on the sphere. The algorithm of subdivision can be described as follows: (1) starting from Level-0, obtain the vertex coordinates and facet information, i.e., which three vertices make up a triangle; (2) find the edge information from the facet information; (3) take the midpoints of the edges as the new vertices for the next level of grids; (4) find the facet information of the next level of grids. As such, we can find the vertex and facet information for arbitrarily high levels of grids. It turns out that the number of grid points of a particular level J is $N_J = 4^J N_0 - 2(4^J - 1)$, where N_0 $(= 12)$ is the number of zero-level grid points. In the appendix, we provide a detailed description on how to obtain the hierarchical geodesic grids.

2.2. The global and local naming scheme

Before we introduce the lifting scheme, it is important to clarify the notations with respect to the grid points. Since each grid point on the sphere is associated with a particular direction, we can use a set of unit vectors to denote the grid points, i.e.,

$$\mathbf{K}^j = \{\hat{k}_i^j\}, i = 1, 2, \ldots, N_j. \tag{1}$$

By subdivision (see the Appendix), we obtain the new grid points by taking the midpoints of the edges in level j. These new grid points, together with the grid points of level j, make up the set of grid points of level $(j+1)$. We denote the new grid points obtained in level j by,

$$\mathbf{M}^j = \{\hat{m}_i^j\}, i = 1, 2, \ldots, M_j. \tag{2}$$

For obvious reasons, we have

$$\mathbf{K}^{j+1} = \mathbf{K}^j \cup \mathbf{M}^j. \tag{3}$$

The notations described above constitute the global naming scheme for the grid points on the sphere. Because a wavelet function is localized, it is also helpful to introduce the local naming scheme associated with the local grid points for wavelet transform. Fig. 2 illustrates a local naming scheme of the grid points, which will be used to describe the wavelet transform. The figure

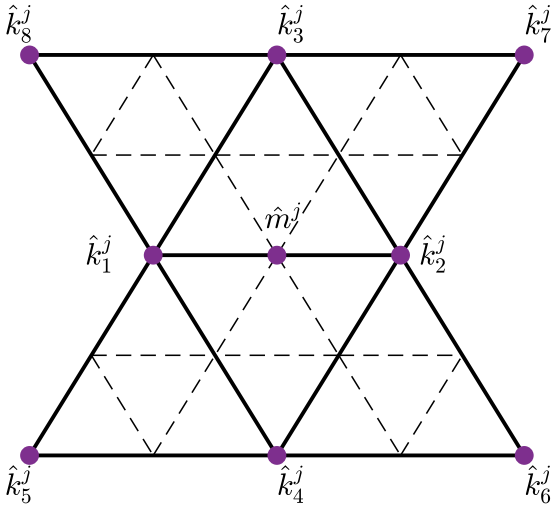

Fig. 2. Local naming scheme for wavelet transform.

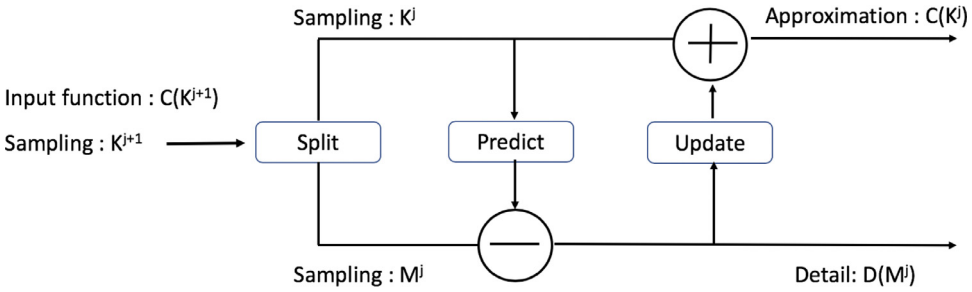

Fig. 3. The lifting scheme for forward wavelet transform.

displays a particular point $\hat{m}^j$ in the middle, and some of its neighborhood $\{\hat{k}_i^j\}$, $i = 1, 2, \ldots, 8$. The dashed lines connect the midpoints of the vertices of level-j. We denote the set of local neighborhood of point $\hat{m}^j$ by,

$$\mathbf{B}(\hat{m}^j) = \{\hat{k}_i^j\}, i = 1, 2, \ldots, 8. \tag{4}$$

For obvious reasons, we have

$$\mathbf{B}(\hat{m}^j) \subset \mathbf{K}^j, \hat{m}^j \in \mathbf{M}^j. \tag{5}$$

2.3. The lifting scheme

A recursive partition of the sphere provides different levels of grid points, on which a function can be evaluated. Intuitively, the evaluation of a function using different levels of grid points can be seen as the multi-scale representation of the function, or signal. The basic idea of wavelet transform is to exploit the correlation structure within the signal with multi-scale representations. The correlation structure is often local, both spatially and spectrally. The lifting scheme is an effective method for constructing wavelets on the sphere, relying on pure spatial manipulation. To some extent, it is more intuitive than classical wavelet analysis, as there is no Fourier transform involved.

Let us begin with introducing the forward transform, as the inverse transform is exactly the reverse process. The forward wavelet transform starts from the finest level of grid, J, to the coarsest level of grid, J_0, whereas the inverse transform goes backward. There are three basic steps in the lifting scheme, namely the split, predict and update. Let a spherical function be evaluated on the grid of level $(j+1)$, denoted as $C(\mathbf{K}^{j+1})$. Using the relation of Eq. (3), we can represent the function as the union of two functions, namely,

$$C(\mathbf{K}^{j+1}) = C(\mathbf{K}^j) \cup C(\mathbf{M}^j). \tag{6}$$

This is the split process. The split step has done nothing to function F, simply identifying the samples on $\mathbf{K}^j$ and $\mathbf{M}^j$. It is expected that $C(\mathbf{K}^j)$ and $C(\mathbf{M}^j)$ will have some correlations because $\mathbf{M}^j$ is generated by selecting the midpoints of edges of $\mathbf{K}^j$. To quantify the correlations, we try to predict $C(\mathbf{M}^j)$ from $C(\mathbf{K}^j)$, i.e.,

$$D(\mathbf{M}^j) = C(\mathbf{M}^j) - \mathbb{P}(C(\mathbf{K}^j)). \tag{7}$$

This is the predict process. $\mathbb{P}$ is called a predictor, and $D(\mathbf{M}^j)$ are the differences between $C(\mathbf{M}^j)$ and its prediction from $C(\mathbf{K}^j)$. The predictor is local, making use of the neighbours of each point in $\mathbf{M}^j$. If the prediction is good, then $D(\mathbf{M}^j)$ is sparse. $D(\mathbf{M}^j)$ are then called the wavelet coefficients corresponding to grid points in $\mathbf{M}^j$, and $C(\mathbf{K}^j)$ are the scaling function coefficients corresponding to grid points in $\mathbf{K}^j$. Upon prediction, the wavelet coefficients are obtained by taking advantage of local correlations in space domain. Yet, other properties of the wavelet functions, such as localised on frequency domain (vanishing moments, smoothness), have not been taken into account. To ensure that the wavelets have some vanishing moments, we can adjust the scaling function coefficients in accordance with the wavelet coefficients, i.e.,

$$C(\mathbf{K}^j) = C(\mathbf{K}^j) + \mathbb{U}(D(\mathbf{M}^j)). \tag{8}$$

This is the update process. $\mathbb{U}$ is the update operator. The update operator is also local, making use of two endpoints on the parent edge of every point in $\mathbf{M}^j$. The lifting steps result in an approximation of $C(\mathbf{K}^{j+1})$ using $C(\mathbf{K}^j)$, together with its details represented as $D(\mathbf{M}^j)$. Fig. 3 shows the float chart of the three basic steps for forward wavelet transform.

To be more specific, particularly on the predict and update steps, we make use of the point-wise notation.

1. Split.
   - $\forall\ \hat{k}_i^j \in \mathbf{K}^j : c(\hat{k}_i^j) \leftarrow c(\hat{k}_i^{j+1})$.
2. Predict.
   - $\forall\ \hat{m}_l^j \in \mathbf{M}^j : d(\hat{m}_l^j) = c(\hat{k}_l^{j+1}) - \sum_{\hat{k}_i^j \in \mathbf{B}(\hat{m}_l^j)} p_{i,l}^j c(\hat{k}_i^j),\ i = 1, 2, \ldots, 8.$
3. Update
   - $\forall\ \hat{m}_l^j \in \mathbf{M}^j : c(\hat{k}_{l1}^j) = c(\hat{k}_{l1}^j) + u_{l,1}^j d(\hat{m}_l^j)\ ;\ c(\hat{k}_{l2}^j) = c(\hat{k}_{l2}^j) + u_{l,2}^j d(\hat{m}_l^j)$.

The first step indicates a subsampling of $c(\hat{k}_i^{j+1})$. In the second step, we make use of the local naming scheme to explain what $p_{i,l}^j$ is referred to. Because $\hat{k}_i^j \in \mathbf{B}(\hat{m}_l^j)$, we are using the neighbors of $\hat{m}_l^j$, as illustrated in Fig. 2, to predict the value at $\hat{m}_l^j$, and $p_{i,l}^j$, $i = 1, 2, \ldots, 8$ are the coefficients assigned for those neighboring points. We select the butterfly predictor, i.e., $p_{1,l}^j = p_{2,l}^j = \frac{1}{2}$, $p_{3,l}^j = p_{4,l}^j = \frac{1}{8}$, $p_{5,l}^j = p_{6,l}^j = p_{7,l}^j = p_{8,l}^j = -\frac{1}{16}$. In the third step, $\hat{k}_{l1}^j$ and $\hat{k}_{l1}^j$ are two endpoints of the parent edge of $\hat{m}_l^j$. The coefficients $u_{l,1}^j$ and $u_{l,2}^j$ are chosen such that the wavelet has a vanishing integral on the sphere:

$$\int_\Omega \psi_l^j(\Omega) d\Omega = 0, \tag{9}$$

where ψ_l^j is the wavelet function at $\hat{m}_l^j$. We construct the wavelet function using the scaling functions as follows:

$$\psi_l^j = \phi_l^{j+1} - u_{l,1}^j \phi_{l1}^j - u_{l,2}^j \phi_{l2}^j, \tag{10}$$

where ϕ_l^{j+1} is the scaling function at $\hat{k}_l^{j+1}$, and ϕ_{l1}^j, ϕ_{l2}^j corresponds to the scaling functions at $\hat{k}_{l1}^j$ and $\hat{k}_{l1}^j$, respectively. A vanishing integral of wavelet means $u_{l,i}^j = I_l^{j+1}/2I_{li}^j, i = 1, 2$, where I_l^{j+1} denotes the integral of the scaling function ϕ_l^{j+1}, and I_{li}^j denotes the integral of the scaling function ϕ_{li}^j, for $i = 1, 2$.

Split, predict, and update are the three basic steps for forward wavelet transform. The inverse wavelet transform simply reverses these three steps:

1. Reverse Update

- $\forall\ \hat{m}_l^j \in \mathbf{M}^j : c(\hat{k}_{l1}^j) = c(\hat{k}_{l1}^j) - u_{l,1}^j d(\hat{m}_l^j)\ ;\ c(\hat{k}_{l2}^j) = c(\hat{k}_{l2}^j) - u_{l,2}^j d(\hat{m}_l^j)$.

2. Reverse Predict.
   - $\forall\ \hat{m}_l^j \in \mathbf{M}^j : c(\hat{k}_l^{j+1}) = d(\hat{m}_l^j) + \sum_{\hat{k}_i^j \in \mathbf{B}(\hat{m}_l^j)} p_{i,l}^j c(\hat{k}_i^j),\ i = 1, 2, \ldots, 8.$
3. Reverse Split.
   - $\forall\ \hat{k}_i^j \in \mathbf{K}^j : c(\hat{k}_i^{j+1}) \leftarrow c(\hat{k}_i^j)$.

In describing the lifting scheme, we have chosen a simple scaling function, the interpolating scaling function:

$$\phi_l^j(\hat{k}_{l'}^j) = \delta_{l,l'}, \tag{11}$$

meaning that the scaling function is one at the evaluating grid point, and zero elsewhere. As a result, the lifting scheme manipulates the data, and so the coefficients of the wavelets and scaling functions by imposing the properties of these functions. In other words, the lifting scheme does not construct the wavelets directly, instead, their coefficients are generated directly. This makes the lifting scheme faster than other wavelet transform, even though the complexity of the transforms may be equal to $O(N)$, where N is the number of significant coefficients.

3. Representing the radiation field using spherical wavelets and spherical harmonics

The radiative transfer equation reads

$$\frac{dI(\vec{r}, \hat{k})}{ds} = -\sigma_{ext}(\vec{r})(I(\vec{r}, \hat{k}) - J(\vec{r}, \hat{k})), \tag{12}$$

where $I(\vec{r}, \hat{k})$ is the radiance measured at $\vec{r}$ and propagating along $\hat{k}$, $\sigma_{ext}(\vec{r})$ is the extinction coefficient, $J(\vec{r}, \hat{k})$ is the source function, and s is the distance along a propagation direction $\hat{k}$. Neglecting the emission source, we may write the source function J as a scattering integral, i.e.,

$$J(\vec{r}, \hat{k}) = \frac{\omega(\vec{r})}{4\pi} \int_\Omega P(\vec{r}, \hat{k}, \hat{k}') I(\vec{r}, \hat{k}') d\Omega(\hat{k}'), \tag{13}$$

where $P(\vec{r}, \hat{k}, \hat{k}')$ is the scattering phase function for the media with scattering albedo $\omega(\vec{r})$. Assuming that the scattering phase function only depends on the scattering angle Θ, formed by the directions $\hat{k}$ and $\hat{k}'$, according to spherical convolution theorem [29], we have

$$\widehat{J}_{lm}(\vec{r}) = \omega(\vec{r})\widehat{C}_l(\vec{r})\widehat{I}_{lm}(\vec{r}), \tag{14}$$

where $\widehat{J}_{lm}(\vec{r})$, $\widehat{C}_l(\vec{r})$, and $\widehat{I}_{lm}(\vec{r})$ are the spherical harmonics expansion coefficients with degree l and order m for the source function J, scattering phase function P, and radiance I, respectively. In the iteration scheme of SHDOM, the convolution theorem is applied to compute the source function at different locations using the radiance in the form of spherical harmonics. Next, the source function can be converted to the discrete-ordinates domain. Using the source function in the discrete-ordinates domain, one can compute the radiance along a particular direction $\hat{k}$ through the following integration formula, i.e.,

$$I(s) = e^{-\int_0^s \sigma_{ext}(s')ds'} I(0) + \int_0^s e^{-\int_{s'}^s \sigma_{ext}(t)dt} J(s')\sigma_{ext}(s')ds'. \tag{15}$$

The radiance field can then be transformed into the spherical harmonics domain to obtain the new source functions, and so, iteratively obtain the convergence of the radiance field [16]. Thus, the discrete-ordinates sampling and the transformation between the two representations play an important role in the iteration process.

3.1. Sampling the discrete-ordinates with spherical wavelets

We use the spherical wavelets as a tool for discrete-ordinate sampling. The angular dependence of the radiation can be decomposed into a series of wavelets at different scales and positions on the sphere.

$$I(\vartheta, \varphi) = \sum_{\hat{k}_i^{J_0} \in \mathbf{K}^{J_0}} c(\hat{k}_i^{J_0}) \phi_i^{J_0}(\vartheta, \varphi) + \sum_{j=J_0}^{J-1} \sum_{\hat{m}_l^j \in \mathbf{M}^j} d(\hat{m}_l^j) \psi_l^j(\vartheta, \varphi), \tag{16}$$

where $\phi_i^{J_0}(\vartheta, \varphi)$ is the scaling function corresponding to the location $\hat{k}_i^{J_0}$ at the coarsest scale, $\psi_l^j(\vartheta, \varphi)$ is the wavelet function corresponding to $\hat{m}_l^j$ at scale j, $c(\hat{k}_i^{J_0})$ is the scaling function coefficient, and $d(\hat{m}_l^j)$ is the wavelet coefficient. For two spherical functions $a(\Omega)$ and $b(\Omega)$, we define their inner product as

$$\langle a(\Omega), b(\Omega) \rangle = \int_\Omega a(\Omega) b(\Omega) d\Omega. \tag{17}$$

As such, the coefficients can be represented by the following inner products:

$$c(\hat{k}_i^{J_0}) = \left\langle I(\vartheta, \varphi), \tilde{\phi}_i^{J_0}(\vartheta, \varphi) \right\rangle, d(\hat{m}_l^j) = \left\langle I(\vartheta, \varphi), \tilde{\psi}_l^j(\vartheta, \varphi) \right\rangle, \tag{18}$$

where $\tilde{\phi}_i^{J_0}(\vartheta, \varphi)$ and $\tilde{\psi}_l^j(\vartheta, \varphi)$ are the corresponding dual scaling function and dual wavelet function. Eq. (16) and Eq. (18) are the general expressions for the wavelet transform. The forward wavelet transform (Eq. (18)) computes the coefficients, and the inverse wavelet transform (Eq. (16)) reconstructs the signal from the obtained coefficients. The lifting scheme, as explained in Section 2, is an efficient way of performing the wavelet transform on the sphere [30–32].

Note that, if the coefficient of a wavelet is very small, it can be set to zero without introducing much difference to the original signal. In signal processing, such an operation is called thresholding, which leads to data compression. Notice that, as coefficients are defined on particular grid points, they also represent the weights of these grid points. Therefore, the absolute values of these coefficients can be used as a criterion for selecting important grid points. This is the reason why we can use the spherical wavelet as an adaptive discrete sampling tool.

3.2. Spherical harmonics expansion

The directional dependence of radiance can be also represented using spherical harmonics up to a particular degree :

$$I(\vartheta, \varphi) = \sum_{l=1}^{L} \sum_{m=-l}^{l} \widehat{I}_{lm} Y_{lm}(\vartheta, \varphi). \tag{19}$$

In this study, we apply the real-valued form of the orthonormal spherical-harmonics basis functions, i.e.,

$$Y_{lm}(\vartheta, \varphi) = \sqrt{\frac{2l+1}{4\pi} \frac{(l-|m|)!}{(l+|m|)!}} P_{l|m|}(\cos\vartheta) N_m(\varphi), \tag{20}$$

where $N_m(\varphi)$ is

$$N_m(\varphi) = \begin{cases} \sqrt{2}\cos(m\varphi), & \text{if } m > 0, \\ 1, & \text{if } m = 0, \\ \sqrt{2}\sin(|m|\varphi), & \text{if } m < 0. \end{cases} \tag{21}$$

The $P_{l|m|}(cos\vartheta)$ functions are the associated Legendre functions:

$$P_{lm}(x) = \frac{1}{2^l l!}(1-x^2)^{m/2} \frac{d^{l+m}}{dx^{l+m}}(x^2-1)^l. \tag{22}$$

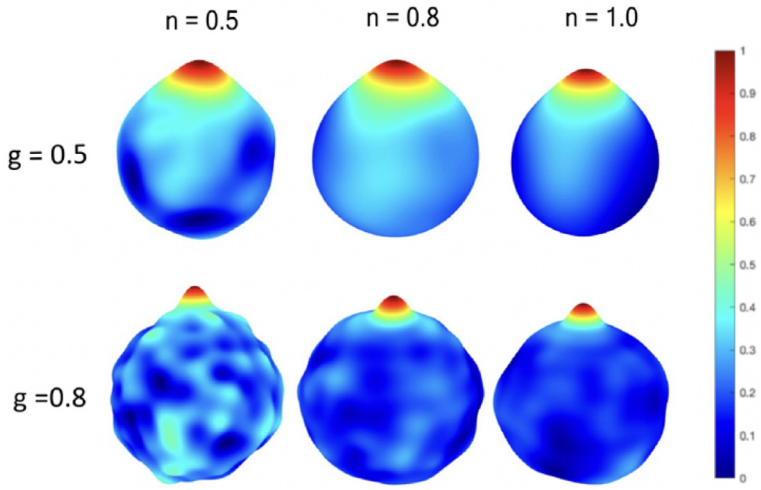

Fig. 4. Band-limited radiation fields with different parameters.

Table 1
The number of grid points for different levels J.

J	0	1	2	3	4	5	6	7	8
N_J	12	42	162	642	2562	10,242	40,962	163,842	655,362

3.3. Band-limited radiation fields

In order to investigate the representation of the radiation fields, we shall construct a formula for numerical analysis purposes. We apply the testing radiation fields in terms of the spherical-harmonics coefficients:

$$\widehat{I}_{lm} = \begin{cases} g^{0.5l}, & \text{if } m = 0, \\ \frac{1}{2} g^{nl} x, & \text{if } m \neq 0, \end{cases} \tag{23}$$

where x is a Gaussian random variable with zero mean and unit standard deviation, n is set to be a number larger than 0.5, so that the coefficients for $m \neq 0$ decrease faster towards higher degree l. And g is the asymmetry factor of the Henyey–Greenstein scattering phase functions:

$$P_{HG}(\Theta) = \frac{(1-g^2)}{(1-2g\cos(\Theta)+g^2)^{3/2}} = \sum_{l=0}^{\infty} (2l+1) g^l P_l(\Theta). \tag{24}$$

The formula is motivated by the spherical convolution theorem for the iterative computation of source function [16,29]. The characteristics of this function are determined by three parameters, i.e., the highest degree L, asymmetry factor g, and number n for the case $m \neq 0$. It mimics the forward peak of the radiation fields and the randomness induced by the scattering media. Fig. 2 displays some examples of fields generated with selected g, n, and a fixed degree $L = 20$. These fields can be seen as the directional distribution of radiance within a cloud of particles with the collimated source illuminating from the bottom. The values of the functions are normalised to their corresponding maximum values. As the number n becomes larger, the smoothness of field increases, which also mimics the iterative process towards the convergence in the simulation. It should be noted that, in contrast to the Gaussian random sphere construction [33], this function is not everywhere positive-definite (although, it is almost everywhere positive-definite). Its construction is mathematically-driven and does not correspond to any particular physical field (Fig. 4).

3.4. The transformation between two representations

In this section, we present a method for evaluating the differences between the spherical wavelet and spherical harmonics representations of the radiation field. With the two transforms, the directional dependence of radiance is encoded in wavelet coefficients and harmonics coefficients, respectively. Since the wavelet coefficients are defined at particular grid points, the number of wavelet coefficients is equal to the number of grid points N_J (the scaling function is also called the unlifted wavelet, see [21]). Table 1 lists some values of N_J.

It can be seen that N_J increases quite fast with J. On the other hand, the number of coefficients used in the spherical-harmonics representations increase with L in the form of $(L+1)^2$. For comparison, Table 2 lists the number of coefficients for a selection of degrees.

Consider the following system of equations, relating the discrete-ordinate representation of level-J with the spherical-harmonics representation of degree-L.

$$\begin{bmatrix} I(\hat{k}_1) \\ I(\hat{k}_2) \\ \vdots \\ I(\hat{k}_{N_J}) \end{bmatrix} = \begin{bmatrix} Y_1(\hat{k}_1) & Y_2(\hat{k}_1) & \dots & Y_{(L+1)^2}(\hat{k}_1) \\ Y_1(\hat{k}_2) & Y_2(\hat{k}_2) & \dots & Y_{(L+1)^2}(\hat{k}_2) \\ \vdots & \vdots & \vdots & \vdots \\ Y_1(\hat{k}_{N_J}) & Y_2(\hat{k}_{N_J}) & \dots & Y_{(L+1)^2}(\hat{k}_{N_J}) \end{bmatrix} \begin{bmatrix} \widehat{I}_1 \\ \widehat{I}_2 \\ \vdots \\ \widehat{I}_{(L+1)^2} \end{bmatrix} \tag{25}$$

Note the indices of the spherical-harmonics basis functions have been re-ordered. Let X_{SH}^L be the column vector of spherical har-

Table 2
The number of spherical-harmonics coefficients for a selection of degrees.

L	0	10	20	30	40	50	60	70	80	90	100
$(L+1)^2$	1	121	441	961	1681	2601	3721	5041	6561	8281	10,201

monics coefficients, I^J_{DO} be the discrete-ordinate radiance vector sampled at level-J, and A_{JL} be the transformation matrix. Then Eq. (25) gives the expression of the discrete-ordinate radiance,

$$I^J_{DO} = A_{JL} X^L_{SH}. \tag{26}$$

The least-squares solution of this equation, i.e.,

$$\widetilde{X}^L_{SH} = \arg\min_X \left\| I^J_{DO} - A_{JL} X \right\|, \tag{27}$$

is

$$\widetilde{X}^L_{SH} = A^\dagger_{JL} I^J_{DO}, \tag{28}$$

where

$$A^\dagger_{JL} = (A^T_{JL} A_{JL})^{-1} A^T_{JL} \tag{29}$$

is the pseudoinvese computed by Singular Value Decomposition (SVD) [34]. Note that A_{JL} and $A^\dagger_{JL}$ are completely determined by the chosen grid points, $\mathbf{K}_J$, and spherical harmonics degree L. The spherical wavelets help us find a new set of directions, $\mathbf{U}^J$, as a subset of $\mathbf{K}^J$:

$$\mathbf{K}^J \supset \mathbf{U}^J = \{\hat{u}_i\}, i = 1, 2, \ldots, N_u, \tag{30}$$

by performing forward wavelet transform starting from level-J. At a result, one can construct a transformation matrix using $\mathbf{U}^J$, denoted as U_{JL}, and so, find the corresponding discrete-ordinate approximations and least-squares solutions:

$$I^U_{DO} = U_{JL} X^L_{SH}, \tag{31}$$

$$\widetilde{X}^L_{SH} = U^\dagger_{JL} I^U_{DO}. \tag{32}$$

Eq. (26) together with Eq. (28) are called the non-adaptive transformations under A_{JL} and $A^\dagger_{JL}$. Eqs. (31) and (32) are called the adaptive transformations under U_{JL} and $U^\dagger_{JL}$. Obviously, U_{JL} is a submatrix of A_{JL} by reducing some rows.

Note that $\widetilde{X}^L_{SH} \neq X^L_{SH}$. The discrete-ordinate radiance of level-J' corresponding to $\widetilde{X}^L_{SH}$ is

$$\widetilde{I}^{J'}_{DO} = A_{J'L} \widetilde{X}^L_{SH}. \tag{33}$$

Let $\#(\widetilde{I}^{J'}_{DO})$ denote the number of elements in $\widetilde{I}^{J'}_{DO}$. We define the *error in discrete-ordinate radiance space* as,

$$\varepsilon^{J'}_{DO}(\widetilde{X}^L_{SH}) = \frac{1}{\#(\widetilde{I}^{J'}_{DO})} \left\| \widetilde{I}^{J'}_{DO} - I^{J'}_{DO} \right\| = \frac{1}{\#(I^{J'}_{DO})} \left\| A_{J'L} \widetilde{X}^L_{SH} - A_{J'L} X^L_{SH} \right\|. \tag{34}$$

$\varepsilon^{J'}_{DO}(\widetilde{X}^L_{SH})$ evaluates the *error* with respect to $\widetilde{X}^L_{SH}$ using the grid of level-J'. Using J' is because the evaluation of the *error* with respect to $\widetilde{X}^L_{SH}$ is independent of computing $\widetilde{X}^L_{SH}$, and so, one may use a different level of grid.

4. Numerical results

Given a spherical harmonics degree L, a natural question is how to determine the number and locations of the discrete-ordinate samples. Theoretical investigation of this question is beyond the scope of this study. Here we focus on investigating this question via some numerical experiments using the non-adaptive and adaptive transformations.

4.1. Non-adaptive transformations

The procedure of the numerical experiments is as follows: for $L = 4, 5, \ldots, 40$, and $J = 1, 2, \ldots, 5$, perform the following steps to obtain the *error* terms,

1. Generate the vector X^L_{SH} of length $(L+1)^2$.
2. Construct the transformation matrix A_{JL}, and compute the discrete-ordinate radiance vector $I^J_{DO} = A_{JL} X^L_{SH}$.
3. Compute $\widetilde{X}^L_{SH} = A^\dagger_{JL} I^J_{DO}$.

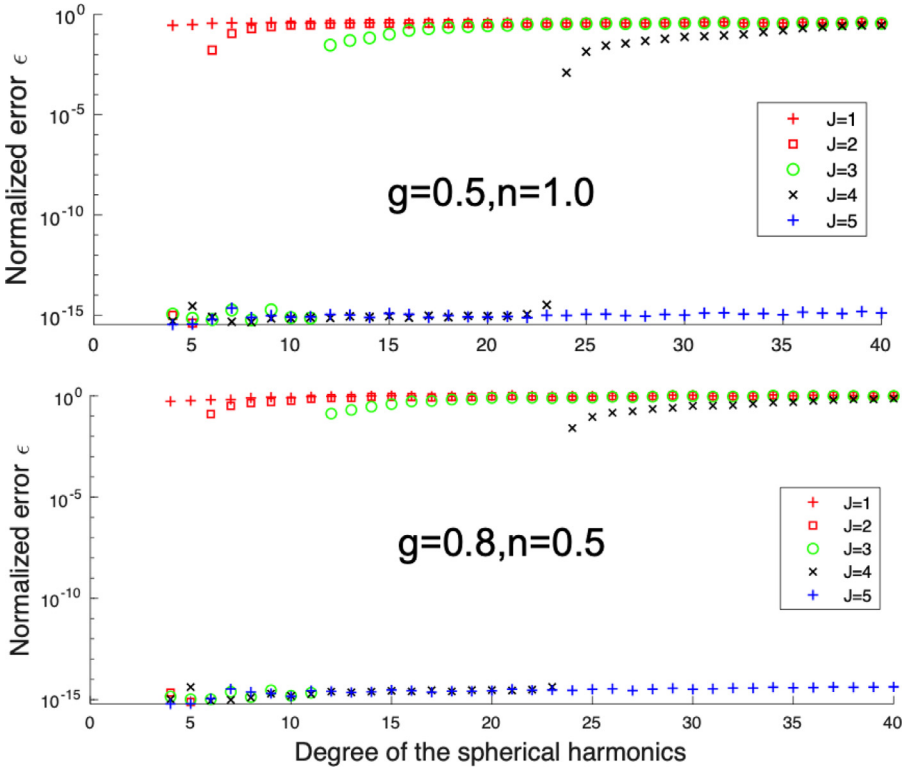

Fig. 5. The normalized error term as a function of the highest degree. The upper one is the distribution with $g = 0.5$ and $n = 1.0$, and the lower one is the distribution with $g = 0.8$, and $n = 0.5$.

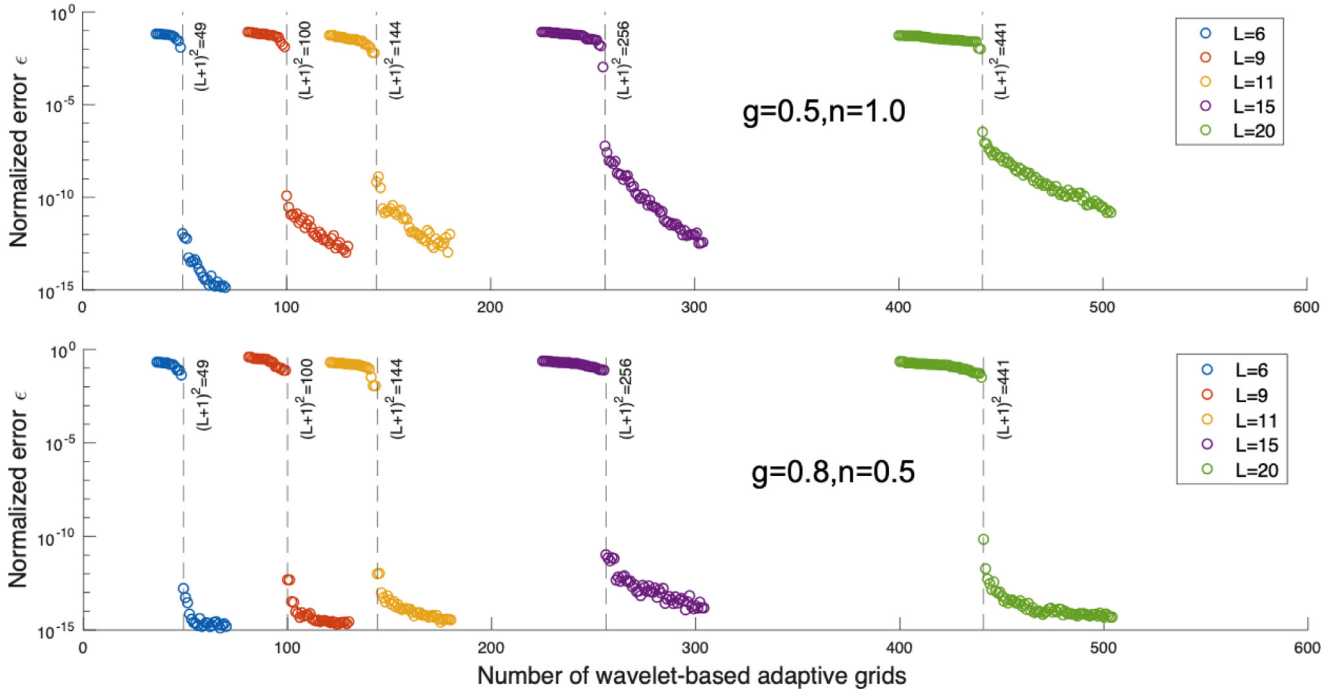

Fig. 6. The normalized error term as a function N_u for a selection of L. The upper one is the case of $g = 0.5$ and $n = 1.0$, and the lower one is case of $g = 0.8$, and $n = 0.5$.

4. Construct the transformation matrix $A_{J'L}$ at level-$J' = 5$ and compute the *error* term $\varepsilon^{J'}_{DO}(\widetilde{X}^L_{SH})$ using Eq. (34).

Fig. 5 displays the *error* as a function of L for the selected J.

It can be seen that because the sampled grid points are non-adaptive, it will inevitably cause two problems:

1. The number of grid points is too small to obtain high accuracy (such as $J = 1$);
2. The number of grid points is too large, and the efficiency of the computation becomes low (such as $J = 5$).

4.2. Wavelet-based adaptive transformations

An important difference between the spherical-harmonics and spherical-wavelets representations is that the former is global and the latter is local. Due to the property of localisation, the coefficient of a wavelet also suggests the weight of particular location. Roughly speaking, if a wavelet coefficient is small, the information contained at that particular grid point is well represented by its neighbouring points. Thus, one can remove some of the grid points with small coefficients, which leads to what we called the adaptive representation. The principle can be stated using the following approximation:

$$I(\vartheta,\varphi) = \sum_{\hat{k}_i^{J_0}\in\mathbf{K}^{J_0}} c(\hat{k}_i^{J_0})\phi_i^{J_0}(\vartheta,\varphi) + \sum_{j=J_0}^{J-1}\sum_{\hat{m}_l^j\in\mathbf{M}^j} d(\hat{m}_l^j)\psi_l^j(\vartheta,\varphi), \quad (35)$$

$$\approx \sum_{\hat{k}_i^{J_0}\in\mathbf{K}^{J_0}} c(\hat{k}_i^{J_0})\phi_i^{J_0}(\vartheta,\varphi) + \sum_{j=J_0}^{J-1}\sum_{\hat{m}_l^j\in\mathbf{M}^j,\left|d(\hat{m}_l^j)\right|>t} d(\hat{m}_l^j)\psi_l^j(\vartheta,\varphi), \quad (36)$$

where t is the "tolerance" for this approximation. If the approximation is satisfactory, we may use a smaller amount of grid points to represent the original function, which is similar to the truncation of the higher level grids.

To examine this, we perform the following numerical experiments: for $L = 6, 9, 11, 15, 20$, and $J = 5$,

1. Generate the vector X^L_{SH} of length $(L+1)^2$.
2. Construct the transformation matrix A_{JL}, and compute the discrete-ordinate radiance vector $I^J_{DO} = A_{JL}X^L_{SH}$.
3. Apply wavelet transform to I^J_{DO}, i.e., compute the wavelet coefficients, $c(\hat{k}_i^{J_0})$ for all $\hat{k}_i^{J_0}\in\mathbf{K}^{J_0}$, and $d(\hat{m}_l^j)$ all for $\hat{m}_l^j\in\mathbf{M}^j$, $j = J_0, 1, \ldots, J-1$.
4. Select $N_u \approx (L+1)^2$ grid points with the largest wavelet coefficients to from a set of grid points, $\mathbf{U}^J = \{\hat{u}_i\}, i = 1, 2, \ldots, N_u$. Construct the transformation matrix U_{JL} using U^J.
5. Compute the discrete-ordinate radiance using $I^U_{DO} = U_{JL}X^L_{SH}$, and recover the coefficients by $\widetilde{X}^L_{SH} = U^\dagger_{JL}I^U_{DO}$.
6. Compute the error term $\varepsilon^{J'}_{DO}(\widetilde{X}^L_{SH})$ using $J' = 5$ in Eq. (34).

As a result, for each L, we will find approximately $(L+1)^2$ adaptive grid points, which is the total number of spherical harmonics coefficients. Fig. 6 displays the *error* term as a function of N_u for a selection of L. It can be seen that there is a criti-

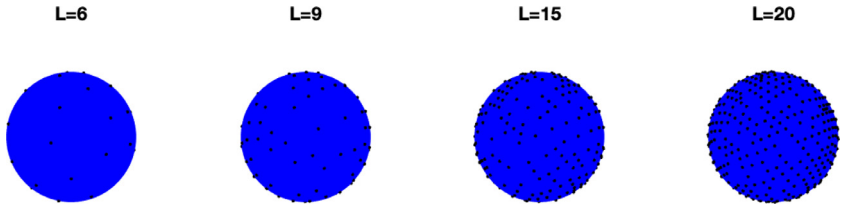

Fig. 7. Wavelet-based adaptive grid points for selected degrees. The radiation field parameters are $g = 0.5$ and $n = 0.5$.

cal line $x_c = (L+1)^2$ of error transition, meaning for a number of adaptive grid points $N_u > x_c$, the error will be reduced dramatically. With wavelet transform, we can capture this critical line by selecting the appropriate discrete ordinates based on the magnitudes of their corresponding coefficients. The reduced transformation matrices U_{JL} and $U_{JL}^{\dagger}$ turn out to have a much smaller size than the original transformation matrices A_{JL} and $A_{JL}^{\dagger}$. This makes the transformation between the two representations accurate and efficient. Fig. 7 displays an example of the wavelet-based adaptive grid points with a size around the critical line of $x_c = (L+1)^2$.

5. Concluding remarks

Representing the radiation fields is the first step towards the solutions of radiative transfer problems. We introduce the spherical wavelets as a numerical tool to represent the radiation fields. We compare the spherical-wavelets method with the commonly applied spherical-harmonics method, investigating their transformation error and efficiency using a parameterised function mimicking the characteristics of the radiation field. The characteristics of the method include the following: first, it can provide adaptivity in selecting propagation directions; second, the number of sampled grid points is around $(L+1)^2$, which is equal to the number of spherical harmonics coefficients; third, the complexity of the wavelet transform is $O(N)$, where N is the number of significant wavelet coefficients.

Compared to the current popular methods, the spherical wavelets provide a unique way of representing spherical functions. Despite that we apply the spherical wavelets as a discrete sampling tool on the sphere, and its potential is yet to be explored. The lifting scheme is just one way to construct the wavelets on the sphere, there are some other ways to perform wavelets transform, particularly, in a continuous setting. Based on the lifting scheme, we take advantages of the magnitude of the coefficients for adaptive representation, whereas for continuous wavelet transform, one may also take advantage of the properties of the wavelet functions for modeling the radiation fields. This may deserve to be studied in the future. Our goal is to develop solution methods which can have both the advantages of discrete-ordinate-based and spherical-harmonics- based methods. With the spherical-harmonics representations, we have the analyticity and fast integration; with the discrete-ordinates representations, one can compute and update the fields in a flexible and adaptive way, and this is often beneficial for dealing with complex 3-D media. The results demonstrate the feasibility of using the spherical wavelets to obtain adaptive radiation propagation directions. In future work, we shall combine the spherical harmonics and spherical wavelets to solve radiative transfer problems in realistic 3-D media.

Declaration of Competing interests

None.

CRediT authorship contribution statement

Guanglang Xu: Conceptualization, Methodology, Software, Writing - original draft. **Karri Muinonen:** Supervision, Writing - review & editing.

Acknowledgment

This work was supported by the Academy of Finland Consortium Project Albedo under Project 298137 and Project 298139.

Appendix A

In this appendix, we give a more detailed description on how to subdivide the grids on the sphere recursively. A nice reference for subdivision is [35]. The information that describes a particular level of grids include: 1. the vertex coordinates on the spherical surface; 2. A matrix of indices that tell which three vertices make up a triangle. The subdivision algorithm finds the next level of grid information based on the previous level. Starting from the 0-level grids, icosahedron, the vertex coordinates and facet indices can be stored in two matrices, i.e.,

$$V = \begin{pmatrix} x_1, x_2, \ldots, x_{N_v} \\ y_1, y_2, \ldots, y_{N_v} \\ z_1, z_2, \ldots, z_{N_v} \end{pmatrix} = \begin{pmatrix} \mathbf{x} \\ \mathbf{y} \\ \mathbf{z} \end{pmatrix}, \tag{37}$$

$$F = \begin{pmatrix} f_{1,a}, f_{2,a}, \ldots, f_{N_f,a} \\ f_{1,b}, f_{2,b}, \ldots, f_{N_f,b} \\ f_{1,c}, f_{2,c}, \ldots, f_{N_f,c} \end{pmatrix} = \begin{pmatrix} \mathbf{f}_a \\ \mathbf{f}_b \\ \mathbf{f}_c. \end{pmatrix}. \tag{38}$$

By finding unique combinations of two vertices in all facets, we can find the indices of all edges of the 0-level grids, and, store them in a 2 by N_e matrix, i.e.,

$$E = \begin{pmatrix} e_{l,1}, & e_{l,2} & , \ldots, & e_{l,N_e} \\ e_{r,1}, & e_{r,2} & , \ldots, & e_{r,N_e} \end{pmatrix} = \begin{pmatrix} \mathbf{e}_l \\ \mathbf{e}_r \end{pmatrix}. \tag{39}$$

Fig. A.8 illustrates the facet and edge information (index matrix) stored in the matrices of F and E. Because E stores the indices associated with V, there is a mapping relation between E and V. Making use of the above notations, we can generate two matrices similar to V, storing the vertices coordinates associated with l and r points respectively, i.e.,

$$V_l = \begin{pmatrix} \mathbf{x} \\ \mathbf{y} \\ \mathbf{z} \end{pmatrix}_{\mathbf{e}_l}; V_r = \begin{pmatrix} \mathbf{x} \\ \mathbf{y} \\ \mathbf{z} \end{pmatrix}_{\mathbf{e}_r}. \tag{40}$$

The size of V_l or V_r is 3 by N_e, because the length of the index vector is N_e. The coordinates of the new vertices can be computed by

$$V_m = \frac{1}{2}(V_l + V_r). \tag{41}$$

The vertex coordinates of the next level can be stored in a new matrix of size 3 by $(N_v + N_e)$, i.e.,

$$V_{new} = (V, V_m). \tag{42}$$

The subdivision algorithm divides one triangle into four, as illustrated in Fig. A.9.

The next aim is to construct the matrix F_{new}, which stores facet indices of the next level grid, i.e,

$$F_{new} = \begin{pmatrix} \mathbf{f}_a, & \mathbf{f}_b, & \mathbf{f}_c, & \mathbf{f}_e \\ \mathbf{f}_e, & \mathbf{f}_f, & \mathbf{f}_g, & \mathbf{f}_f \\ \mathbf{f}_g, & \mathbf{f}_e, & \mathbf{f}_f, & \mathbf{f}_g \end{pmatrix}. \tag{43}$$

Note that the indices of the new vertices $\mathbf{f}_e$, $\mathbf{f}_f$, $\mathbf{f}_g$ correspond to the edges made by

$$\begin{pmatrix} \mathbf{f}_a \\ \mathbf{f}_b \end{pmatrix}, \begin{pmatrix} \mathbf{f}_b \\ \mathbf{f}_c \end{pmatrix}, \begin{pmatrix} \mathbf{f}_a \\ \mathbf{f}_c \end{pmatrix}. \tag{44}$$

Because the order of the new vertices is determined by how we arrange the edges, we may construct a N *by* N sparse, symmetry matrix, storing the relation between the index of the edges and the index of the new vertices, i.e.,

$$S[e_{l,k}; e_{r,k}] = S[e_{r,k}; e_{l,k}] = N + k, k = 1, 2, \ldots, N_e. \tag{45}$$

By making using of this sparse matrix, we can conveniently obtain $\mathbf{f}_e$, $\mathbf{f}_f$, $\mathbf{f}_g$ by the following equations,

$$\mathbf{f}_e = S[\mathbf{f}_a; \mathbf{f}_b], \tag{46}$$

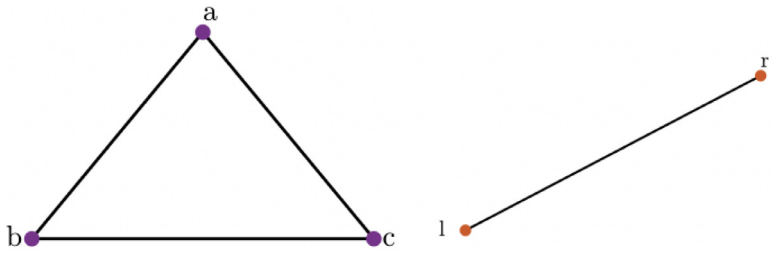

Fig. A1. The facet and edge information stored in matrices *F* and *E*.

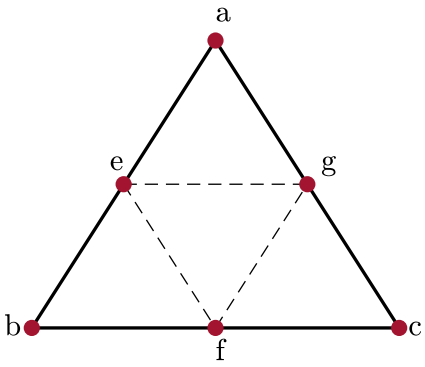

Fig. A2. Four small triangles are generated from one by subdivision.

$$\mathbf{f}_f = S[\mathbf{f}_b; \mathbf{f}_c], \tag{47}$$

$$\mathbf{f}_g = S[\mathbf{f}_c; \mathbf{f}_a]. \tag{48}$$

As such, we complete the task of obtaining the new vertex and facet information from the previous level of information, i.e.,

$$(V, F) \rightarrow (V_{new}, F_{new}). \tag{49}$$

References

[1] Thomas GE, Stamnes K. Radiative transfer in the atmosphere and ocean. Cambridge University Press; 2002.
[2] Kourganoff V. Basic methods in transfer problems; radiative equilibrium and neutron diffusion. Oxford, Clarendon Press; 1952.
[3] Liou K-N. An introduction to atmospheric radiation, 84. Elsevier; 2002.
[4] Iwabuchi H. Efficient monte carlo methods for radiative transfer modeling. JAtmos. Sci 2006;63(9):2324–39.
[5] Ramon D, Steinmetz F, Jolivet D, Compiègne M, Frouin R. Modeling polarized radiative transfer in the ocean-atmosphere system with the gpu-accelerated smart-g monte carlo code. J Quant Spectrosc Radiative Transfer 2019;222:89–107.
[6] Lyapustin AI. Radiative transfer code sharm for atmospheric and terrestrial applications. Appl Opt 2005;44(36):7764–72. doi:10.1364/AO.44.007764.
[7] Ishida H, Asano S. A finite-volume solution with a bidirectional upwind difference scheme for the three-dimensional radiative transfer equation. J Atmos Sci 2007;64(11):4098–112.
[8] Spurr R. Lidort and vlidort: Linearized pseudo-spherical scalar and vector discrete ordinate radiative transfer models for use in remote sensing retrieval problems. In: Light Scattering Reviews 3. Springer; 2008. p. 229–75.
[9] Stamnes K, Tsay S-C, Wiscombe W, Jayaweera K. Numerically stable algorithm for discrete-ordinate-method radiative transfer in multiple scattering and emitting layered media. ApplOpt 1988;27(12):2502–9.
[10] Rozanov A, Rozanov V, Buchwitz M, Kokhanovsky A, Burrows J. Sciatran 2.0–a new radiative transfer model for geophysical applications in the 175–2400 nm spectral region. Adv Space Res 2005;36(5):1015–19.
[11] Ota Y, Higurashi A, Nakajima T, Yokota T. Matrix formulations of radiative transfer including the polarization effect in a coupled atmosphere–ocean system. J Quant Spectrosc Radiative Transfer 2010;111(6):878–94.
[12] Khan T, Thomas A. On derivation of the radiative transfer equation and its spherical harmonics approximation for scattering media with spatially varying refractive indices. Technical Report. Clemson University Mathematical Sciences; 2004.
[13] Ou S-CS, Liou K-N. Generalization of the spherical harmonic method to radiative transfer in multi-dimensional space. J Quant Spectrosc Radiative Transfer 1982;28(4):271–88.
[14] Chandrasekhar S. Radiative Transfer. Courier Corporation; 1960. 56, Eq. (3)
[15] Chai JC, Lee HS, Patankar SV. Ray effect and false scattering in the discrete ordinates method. Numer Heat Transfer Part B Fundam 1993;24(4):373–89.
[16] Evans KF. The spherical harmonics discrete ordinate method for three-dimensional atmospheric radiative transfer. J Atmos Sci 1998;55(3):429–46.
[17] Evans KF. Two-dimensional radiative transfer in cloudy atmospheres: the spherical harmonic spatial grid method. JAtmosSci 1993;50(18):3111–24.
[18] Evans KF. Shdomppda: a radiative transfer model for cloudy sky data assimilation. J Atmos Sci 2007;64(11):3854–64.
[19] Pincus R, Evans KF. Computational cost and accuracy in calculating three-dimensional radiative transfer: results for new implementations of monte carlo and shdom. J Atmos Sci 2009;66(10):3131–46.
[20] Doicu A, Efremenko DS. Linearizations of the spherical harmonic discrete ordinate method (shdom). Atmosphere 2019;10(6):292.
[21] Schröder P, Sweldens W. Spherical wavelets: efficiently representing functions on the sphere. In: Proceedings of the 22nd annual conference on Computer graphics and interactive techniques. ACM; 1995. p. 161–72.
[22] Schröder P, Sweldens W. Spherical wavelets: texture processing. In: Rendering techniques 95. Springer; 1995. p. 252–63.
[23] Xu G, Gritsevich M, Peltoniemi J, Penttilä A, Wilkman O, Ihalainen O, et al. Spectral reflectance processing via local wavelength-direction correlations. IEEE Geosci Remote Sens Lett 2019.
[24] Antoine J-P, Demanet L, Jacques L, Vandergheynst P. Wavelets on the sphere: implementation and approximations. Appl Comput Harmon Anal 2002;13(3):177–200.
[25] Antoine J-P, Roşca D. The wavelet transform on the two-sphere and related manifolds: a review. In: Optical and digital image processing, 7000. International Society for Optics and Photonics; 2008. p. 70000B.
[26] Gabriel P. Toolbox wavelets on meshes. https://www.mathworks.com/matlabcentral/fileexchange/17577-toolbox-wavelets-on-meshes; 2009.
[27] Daubechies I, Sweldens W. Factoring wavelet transforms into lifting steps. J Fourier AnalAppl 1998;4(3):247–69.
[28] Hu S, Trevino J, Salvador C, Sakamoto S, Suzuki Y. Modeling head-related transfer functions with spherical wavelets. Appl Acoust 2019;146:81–8.
[29] Driscoll JR, Healy DM. Computing fourier transforms and convolutions on the 2-sphere. AdvApplMath 1994;15(2):202–50.
[30] Sweldens W. Wavelets and the lifting scheme: a 5 minute tour. ZAMM-Zeitschrift fur Angewandte Mathematik und Mechanik 1996;76(2):41–4.
[31] Sweldens W. The lifting scheme: a custom-design construction of biorthogonal wavelets. ApplComputHarmonAnal 1996;3(2):186–200.
[32] Sweldens W. The lifting scheme: a construction of second generation wavelets. SIAM J MathAnal 1998;29(2):511–46.
[33] Muinonen K, Nousiainen T, Fast P, Lumme K, Peltoniemi J. Light scattering by gaussian random particles: ray optics approximation. J Quant Spectrosc Radiative Transfer 1996;55(5):577–601.
[34] Barata JCA, Hussein MS. The moore–penrose pseudoinverse: a tutorial review of the theory. Braz J Phys 2012;42(1–2):146–65.
[35] Zorin D., Schröder P., DeRose T., Kobbelt L., Levin A., Sweldens W.. Subdivision for modeling and animation, siggraph 2000 course notes. http://www.multires.caltech.edu/pubs/sig00notes.pdf; 2000.